Available online at www.sciencedirect.com
SCIENCE DIRECT®
Computers & Fluids 33 (2004) 1225–1250
computers & fluids
www.elsevier.com/locate/compfluid

Development of boundary conditions for direct numerical simulations of three-dimensional vortex breakdown phenomena in semi-infinite domains

M.R. Ruith [a,b,*], P. Chen [a,c], E. Meiburg [b]

[a] *Department of Aerospace and Mechanical Engineering, University of Southern California, Los Angeles, CA 90089, USA*
[b] *Department of Mechanical and Environmental Engineering, University of California, Santa Barbara, CA 93106, USA*
[c] *Yahoo! Inc., 3400 Central Expressway, Santa Clara, CA 95051, USA*

Received 18 April 2002; received in revised form 20 January 2003; accepted 22 April 2003
Available online 10 February 2004

Abstract

The suitability of various open boundary conditions is evaluated for direct numerical simulations of three-dimensional, incompressible, spatially and temporally evolving, swirling laminar jets in domains that extend to infinity in the downstream and radial direction. From the point of view of specifying conditions at the open boundaries, this class of flows is particularly challenging due to its ability to support traveling waves. Towards this end, several radial boundary conditions are implemented and tested with respect to their ability to conserve local and global mass, to handle low and high entrainment flow, and to avoid the introduction of artificial waves propagating from the boundaries into the interior: a free-slip condition, two types of homogeneous Neumann conditions, and a radiation condition in spirit of the outflow boundary condition. Global mass is conserved automatically within machine accuracy in the free-slip and simple radiation case, while the Neumann conditions require some iterative modification to conserve mass. This yields a computationally less efficient scheme which additionally exhibits poorer conservation properties due to the limited number of iterations. The free-slip condition typically requires the largest radial extent of the computational domain due to its impermeable character which is particularly problematic for the high entrainment flow. Hence, the radiation condition has been found as the most suitable lateral boundary condition for both high and low entrainment jets.

* Corresponding author. Present address: Department of Mechanical and Environmental Engineering, University of California, Santa Barbara, CA 93106, USA.
E-mail addresses: ruith@engineering.ucsb.edu (M.R. Ruith), meiburg@engineering.ucsb.edu (E. Meiburg).

0045-7930/$ - see front matter
doi:10.1016/j.compfluid.2003.04.001

1. Introduction

Vortex breakdown in swirling flows is characterized by an abrupt change in the structure of the nominally axisymmetric core, which gives rise to an internal stagnation point. It represents a crucial element in a variety of technical applications ranging from the stabilization of combustion processes to flows over delta wings. Furthermore, it arises in a number of natural settings such as tornadoes, dust devils and water spouts. In spite of its great importance, a satisfactory understanding of the mechanisms leading to vortex breakdown, and hence the ability to predict it, is still elusive. Hence there is a strong motivation to perform highly accurate, detailed numerical simulations in order to unravel the underlying fluid dynamics. The goal is to obtain well resolved spatial and temporal information about the flow field that can be compared against existing theories and experiments on vortex breakdown, cf. Leibovich [30], Althaus et al. [2], Spall and Snyder [46], Lucca-Negro and O'Doherty [32] among others.

Direct numerical simulations of incompressible, nominally axisymmetric swirling flows are particularly difficult to perform, since such flows are very sensitive to small disturbances. Furthermore, simulating the Navier–Stokes equations in cylindrical coordinates requires special care due to the singular behavior of some terms near the axis. As pointed out by Althaus et al. [2] and Spall et al. [44] this problem is often circumvented by solving the equations in Cartesian coordinates. However, this approach introduces unphysical azimuthal perturbations related to grid orientation effects, which can negatively affect the simulation results.

An additional complication arises when swirling flows in semi-infinite domains are to be simulated. The finite size of the computational domain requires the implementation of open boundaries, at which conditions need to be specified that have a negligible influence on the evolution of the flow in the interior of the domain. As Breuer et al. [12] point out, the formulation of such open boundary conditions requires great care especially for time-dependent swirling flows, since they are capable of supporting propagating waves. This renders it much harder to avoid the introduction of artificial waves that propagate upstream from the outflow boundary. In addition, strong swirl can potentially cause strong local entrainment or outflow in the radial direction. This has to be taken into account when selecting lateral boundary conditions, especially since the transitions among various forms of vortex breakdown are very sensitive to coflow fluctuations.

The formulation of proper upstream inflow conditions has been a matter of discussion as well. Fixed inflow conditions are employed by Kopecky and Torrance [27] and Grabowski and Berger [20] in solving the incompressible, steady, axisymmetric Navier–Stokes equations for swirling, laminar flows in a tube and trailing wing vortices, respectively. Their time independent nature raised some concern (e.g. [30,45]), as it artificially constrains the inflow. Such inflow conditions do not allow for upstream propagating disturbances past the inflow plane, which may represent a serious limitation for swirling flows near criticality thresholds. On the other hand, relaxing the fixed inlet boundary conditions may cause the entire breakdown bubble to leave the computational domain. This issue is addressed independently by Krause [29] and Spall et al. [44], who prescribe the axial velocity component on the lateral boundary. Although these authors provide quite different physical justifications and numerical implementations, both sets of simulations successfully model breakdown in tubes, induced and governed by an a priori known pressure distribution at the lateral wall. The vortex breakdown remains within the computational domain, which enables the authors to conduct simulations over extended time periods and to study dif-

ferent types of breakdown in radially confined flows, cf. the review articles of Spall and Synder [46] and Althaus et al. [2]. They reproduce the three major types of vortex breakdown observed in tube experiments (e.g. [18]), viz. the bubble, helical and double-helical types. Spall and Snyder [46] and Althaus et al. [2] point out that these different modes are obtained by imposing a fixed inflow swirl ratio and varying the freestream axial velocity on the lateral boundaries.

In an attempt to eliminate the dominant dependency of the various breakdown modes on the pressure distribution along the lateral boundary, i.e. on the shape of the tube, recent experiments by Billant et al. [7] and Maxworthy (private communication) employ a pressure-driven water jet discharging into a large tank whose side walls are far removed from the core of the swirling jet. These experiments mimic the case of a nominally axisymmetric jet issuing into a domain that is of infinite extent in the radial and downstream directions (semi-infinite domain).

The goal of the present numerical investigation is to simulate vortex breakdown in semi-infinite domains, in order to be able to compare with the above experiments. Towards this end, we solve the Navier–Stokes equations in cylindrical coordinates. The specific issue addressed in this article is the identification of optimal open boundary conditions for simulations of incompressible, time dependent, and three-dimensional vortex breakdown flows. To summarize the above discussion, such boundary conditions should not give rise to artificial waves propagating from the boundaries into the interior of the domain, either along the core of the jet or perpendicularly to it. They should conserve local and global mass around machine accuracy even for long simulation times, and they should allow for the simulations to be carried out in computational domains that do not have to be excessively large. Finally, they should be suitable for both low and high entrainment flows, they should not affect the global stability of the flowfield, cf. Buell and Huerre [13], and they should be computationally efficient and easy to implement. We discuss the suitability in all of these regards of several different boundary conditions, ranging from free-slip and various homogeneous Neumann conditions to radiation conditions. The advantages and shortcomings of all of the conditions with respect to the above demands will be evaluated in detail.

2. Governing equations

In the present investigation, the incompressible Navier–Stokes equations are formulated in cylindrical coordinates (r, θ, z), cf. Fig. 1. In this formulation, the Navier–Stokes equations exhibit terms of the type r^{-1}, r^{-2}, r^{-3}, which lead to geometrical singularities at the axis $r = 0$. Verzicco and Orlandi [47] propose to rewrite the governing equations by replacing the velocity components

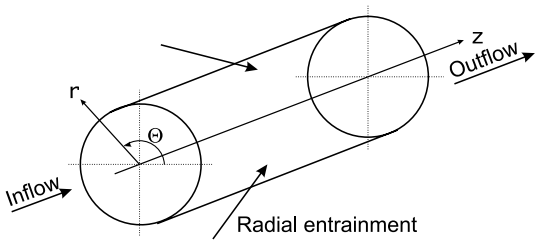

Fig. 1. Sketch of cylindrical computational domain.

v_r, v_θ, v_z with $q_r = v_r \cdot r$, $q_\theta = v_\theta$, and $q_z = v_z$, respectively. Thus $q_r = 0$ per definition on the axis, which on a staggered grid avoids the problem of singularities.

In order to render the governing equations dimensionless, we introduce characteristic length (L) and velocity (U), whose exact form will be discussed below in the context of specific inflow profiles. The convective time scale thus is $T = L/U$, and the characteristic pressure is provided by $P = \rho U^2$, with ρ representing the constant density.

With the above scaling the dimensionless continuity equation becomes

$$\frac{\partial q_\theta}{\partial \theta} + \frac{\partial q_r}{\partial r} + r\frac{\partial q_z}{\partial z} = 0. \tag{1}$$

The non-dimensional momentum equations for constant dynamic viscosity μ follow as

$$\begin{aligned}
\frac{\mathrm{D}q_r}{\mathrm{D}t} &= -r\frac{\partial p}{\partial r} + \frac{1}{Re}\left[r\frac{\partial}{\partial r}\left(\frac{1}{r}\frac{\partial q_r}{\partial r}\right) + \frac{1}{r^2}\frac{\partial^2 q_r}{\partial \theta^2} + \frac{\partial^2 q_r}{\partial z^2} - \frac{2}{r}\frac{\partial q_\theta}{\partial \theta}\right],\\
\frac{\mathrm{D}q_\theta}{\mathrm{D}t} &= -\frac{1}{r}\frac{\partial p}{\partial \theta} + \frac{1}{Re}\left[\frac{1}{r}\left(\frac{\partial}{\partial r}r\frac{\partial q_\theta}{\partial r}\right) - \frac{q_\theta}{r^2} + \frac{1}{r^2}\frac{\partial^2 q_\theta}{\partial \theta^2} + \frac{\partial^2 q_\theta}{\partial z^2} + \frac{2}{r^3}\frac{\partial q_r}{\partial \theta}\right],\\
\frac{\mathrm{D}q_z}{\mathrm{D}t} &= -\frac{\partial p}{\partial z} + \frac{1}{Re}\left[\frac{1}{r}\frac{\partial}{\partial r}\left(r\frac{\partial q_z}{\partial r}\right) + \frac{1}{r^2}\frac{\partial^2 q_z}{\partial \theta^2} + \frac{\partial^2 q_z}{\partial z^2}\right],
\end{aligned} \tag{2}$$

with the substantial derivatives in their conservative form [47]

$$\begin{aligned}
\frac{\mathrm{D}q_r}{\mathrm{D}t} &= \frac{\partial q_r}{\partial t} + \frac{\partial}{\partial r}\left(\frac{q_r^2}{r}\right) + \frac{\partial}{\partial \theta}\left(\frac{q_\theta q_r}{r}\right) + \frac{\partial (q_r q_z)}{\partial z} - q_\theta^2,\\
\frac{\mathrm{D}q_\theta}{\mathrm{D}t} &= \frac{\partial q_\theta}{\partial t} + \frac{1}{r^2}\frac{\partial (r q_\theta q_r)}{\partial r} + \frac{1}{r}\frac{\partial q_\theta^2}{\partial \theta} + \frac{\partial (q_\theta q_z)}{\partial z},\\
\frac{\mathrm{D}q_z}{\mathrm{D}t} &= \frac{\partial q_z}{\partial t} + \frac{1}{r}\frac{\partial (q_r q_z)}{\partial r} + \frac{1}{r}\frac{\partial (q_\theta q_z)}{\partial \theta} + \frac{\partial q_z^2}{\partial z}.
\end{aligned} \tag{3}$$

Here time and pressure are indicated by t and p, respectively. The Reynolds number Re takes its usual form

$$Re = \frac{U \cdot L}{\nu}. \tag{4}$$

The formulation of the non-linear, convective terms is of crucial importance to the numerical stability of the scheme. Apart from time differencing errors, satisfying certain integral constraints is essential for obtaining stable, long term computations ([3,21], etc.). For the fractional-step method employed here, conservation of mass is of superior importance, since the intermediate stage, which is obtained by time advancement of the momentum equations, has to be globally divergence free, as the subsequent projection step modifies only the local divergence.

3. Numerical technique

We employ the finite-difference scheme in primitive variables first introduced by Verzicco and Orlandi [47]. The incompressible, time-dependent, three-dimensional Navier–Stokes equations are

solved in cylindrical coordinates, with second-order spatial accuracy all the way to the axis. The numerical solution is advanced in time by a fractional-step method employing an approximate-factorization technique. The numerical scheme is accelerated by parallelizing the code with MPI.

3.1. Spatio-temporal discretization and accuracy

Chorin [15] as well as Kim and Moin [26] point out that the role of the pressure in the momentum equations can be interpreted as a projection operator, which projects an arbitrary, globally divergence-free velocity field $\hat{v}_i$ into a globally and locally divergence-free velocity field v_i^{l+1}. Here the subscript $i = 1, 2, 3$ refers to the three coordinates r, θ, z, and the superscript $l + 1$ represents the new time level. This fact is exploited by fractional-step methods, also known as time-split methods, which are commonly used in DNS simulations (e.g. [26,38,47]).

Verzicco and Orlandi [47] point out that the implicit treatment of the viscous terms in the momentum equations requires the inversion of large sparse matrices. These matrices can be reduced to three tridiagonal matrices each by an approximate factorization procedure with error $O(\Delta t^3)$, cf. Beam and Warming [5], Kim and Moin [26] for details. Taking the increment $\Delta\hat{q}_i = \hat{q}_i - q_i^l$ the factorized form of the momentum equations reads

$$\begin{aligned}(1 - \vartheta_l A_{ir})(1 - \vartheta_l A_{i\theta})(1 - \vartheta_l A_{iz})\Delta\hat{q}_i = \Delta t[&\gamma_l H_i^l + \varrho_l H_i^{l-1} - G_i(\alpha_l p^l + \beta_l p^{l+1}) \\ &+ (\gamma_l + \varrho_l)(A_{ir} + A_{i\theta} + A_{iz})q_i^l],\end{aligned} \tag{5}$$

with $\vartheta_l = (\gamma_l + \varrho_l)\Delta t/2$. Here H_i contains the spatially discretized convective terms, as well as those viscous terms that have first- or zeroth-order velocity derivatives, while A_{ir}, $A_{i\theta}$ and A_{iz} denote discrete expressions for the viscous terms. G_i represents the discrete gradient in the form

$$G_i = \left(r\frac{\delta}{\delta r}, \frac{1}{r}\frac{\delta}{\delta\theta}, \frac{\delta}{\delta z}\right). \tag{6}$$

Explicit expressions for H_i, G_i, A_{ir}, $A_{i\theta}$ and A_{iz} are obtained by central second-order finite differencing of the momentum equations (2) and (3) on the staggered grid (Fig. 2). Following Harlow and Welch [23], velocity fluxes are defined on the cell surfaces while the pressure p and the variable Φ related to it are defined at the cell centers. Thus only q_r is defined at $r = 0$, with $q_r(r = 0) = 0$ by definition. As a result, second-order accuracy at the axis is retained, since no ad hoc boundary conditions are required at $r = 0$.

Eq. (5) represents a generalization of the equations proposed by Verzicco and Orlandi [47] in the spirit of Armfield and Street [4]. The latter show that, depending on the time integration coefficients α_l, β_l, the fractional-step method may be implemented in an *iterative* ($\alpha_l = 0$, $\beta_l = \gamma_l + \varrho_l \neq 0$), *non-iterative projection* ($\alpha_l = \beta_l = 0$), or *non-iterative pressure correction* ($\alpha_l = \gamma_l + \varrho_l \neq 0$, $\beta_l = 0$) fashion. Note that the subscript l distinguishes the coefficients corresponding to the different substeps of a multi-step method, i.e. $l = 1, 2, 3$ for a three-step method.

Although all types have been implemented in the past, Armfield and Street [4] identify the pressure correction method to be the optimal. They base this decision on the discussion of the boundary conditions for the intermediate velocity flux $\hat{q}_i$. In particular they show for a driven cavity flow that the method retains the temporal order of accuracy without requiring a modified intermediate boundary condition and is computationally efficient, cf. Ruith [40] for further

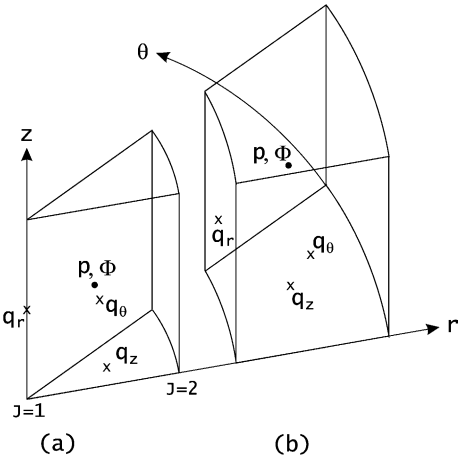

Fig. 2. Sketch of the computational cells: (a) cell at axis and (b) cell in the interior of the domain. p and Φ are defined at the center of the cell, whereas q_θ, q_r and q_z are defined on the cell surfaces.

details. For these reasons we select the pressure correction method, for which Eq. (5) takes the form proposed by Verzicco and Orlandi [47].

In this study we use a three-step hybrid Runge–Kutta/Crank–Nicolson scheme which Rai and Moin [38] attribute to Spalart. It uses an explicit Runge–Kutta method for the convective terms, and an implicit Crank–Nicolson method for the viscous terms. Therefore the numerical scheme exhibits no viscous stability restriction, while the convective time step can be substantially larger for the Runge–Kutta scheme employed if compared to the Adams–Bashforth method traditionally used, cf. Ruith [40] for details. The actual values of the coefficients are $\gamma_1 = 8/15$, $\gamma_2 = 5/12$, $\gamma_3 = 3/4$, $\varrho_1 = 0$, $\varrho_2 = -17/60$ and $\varrho_3 = -5/12$. Due to $\varrho_1 = 0$, the method is self starting. As mentioned above, $\hat{v}_i$ does not satisfy local continuity. This is subsequently enforced in each cell by

$$q_i^{l+1} = \hat{q}_i - (\gamma_l + \varrho_l)\Delta t G_i \Phi, \tag{7}$$

where Φ is a scalar related to the pressure. Substituting Eq. (7) into the continuity equation (1), we obtain a Poisson equation for Φ

$$L\Phi = \frac{1}{(\gamma_l + \varrho_l)\Delta t} D\hat{\mathbf{q}}, \tag{8}$$

with L and D as the discrete Laplace and discrete divergence operators, respectively, in the form

$$D = \frac{1}{r}\frac{\delta}{\delta r} + \frac{1}{r}\frac{\delta}{\delta \theta} + \frac{\delta}{\delta z} \quad \text{and} \quad L = \frac{1}{r}\frac{\delta}{\delta r}\left(r\frac{\delta}{\delta r}\right) + \frac{1}{r^2}\frac{\delta^2}{\delta \theta^2} + \frac{\delta^2}{\delta z^2}. \tag{9}$$

At each substep of the Runge–Kutta scheme the scalar Φ is calculated. The computation of Φ implies the solution of an elliptic equation for which trigonometric expansions are applied in the axial and azimuthal direction. This approach is very efficient for calculating Φ directly, and it gives the solenoidal velocity field within machine round-off errors. Note that no ad hoc boundary conditions need to be specified for Φ since it is defined at the cell center, cf. Fig. 2. However,

compatibility with the velocity boundary conditions requires $\delta\phi/\delta\vec{n} = 0$, with $\vec{n}$ representing the direction perpendicular to the respective boundary, as will be discussed in detail in Section 4.

After Φ is obtained, the velocity is corrected and the pressure is updated by using $Gp^{l+1} = Gp^l + G\Phi - (\gamma_l + \varrho_l)\Delta t/(2Re)LG\Phi$, which is obtained from the discretized momentum equations and transforming $q_i^{l+1} - \hat{q}_i$ with Eq. (7) into Φ. We assume a smooth function Φ so that it is possible to write

$$p^{l+1} = p^l + \Phi - \frac{(\gamma_l + \varrho_l)\Delta t}{2Re} L\Phi. \tag{10}$$

Braza et al. [10] investigate the importance of the viscous term $(\gamma_l + \varrho_l)\Delta t/(2Re)L\Phi$ for the wake behind a circular cylinder and conclude that for high Reynolds number calculations it may be neglected. However, the convergence is improved if one considers the complete Eq. (10) and since the additional computational effort is negligible the viscous term is included in all simulations.

Perot [36,37] shows conclusively that the first-order accuracy of the discrete pressure is inherent to all fractional-step methods of the form $G_i(\alpha_l p^l + \beta_l p^{l+1})$, with $\alpha_l + \beta_l = 1$, independent of the boundary conditions. Moreover, both he as well as Armfield and Street [4] emphasize that the order of accuracy of the pressure update does not affect the order of accuracy of the *incompressible* velocity field. Hence, the present scheme is second order accurate for the viscous terms, and third order accurate for the convective terms. The overall spatial accuracy is second order for the velocity and first order for the pressure.

In the present study we limit ourselves to relatively low Reynolds numbers, i.e. laminar flows. As demonstrated by Verzicco and Orlandi [47], second-order accuracy is satisfactory for this class of flows. In addition, at these moderate Reynolds numbers the high frequency energy content of the flow and the associated aliasing errors can safely be neglected.

3.2. Grid

Since vortex breakdown originates in the vortex core, high spatial resolution is required near the axis. On the other hand, all open boundaries should be sufficiently far removed from the location of the vortex breakdown, in order for it to remain unaffected by the numerical conditions implemented at these boundaries. Furthermore, spatial variations of all flow quantities can be expected to diminish far away from the axis, so that a coarser resolution of the far field is appropriate. For these reasons, a coordinate transformation is attractive that concentrates grid points in the region near the axis. We adopt the radial transformation used by Grabowski and Berger [20] which ensures that successive cells are stretched by a constant factor. It allows to specify the number of points within the vortex core, n_R, and the total number of points in the radial direction n_r used to discretize the entire radial extent of the domain R_d.

In order to avoid any contamination of the vortex breakdown by the downstream boundary, the axial extent of the computational domain Z_d is required to be large. While this will result in weak gradients next to the downstream boundary, we do not employ a mapping of the downstream direction, in order to retain the ability to apply a Fourier series approach for the solution of the Poisson equation (8). To keep the aspect ratio of the computational cells within the vortex core close to 1, a fairly large number of grid points in the axial direction n_z is required. However, this disadvantage is more than compensated by the speed and accuracy of the Poisson solver.

4. Boundary conditions

Fig. 1 shows the three boundaries of the domain: the inflow, outflow and the radial or lateral boundary. In general, all of these boundaries are open, so that mass and momentum can be transported across them. In the following, we will discuss the computational treatment of each of these boundaries separately.

4.1. Inflow boundary

In the present simulations we consider two different inflow profiles, viz. a high and a low entrainment case. Both profiles are axisymmetric and constant over time, and we do not superimpose any perturbations. The use of such steady inflow conditions has been criticized in the context of simulating trailing wing vortices (e.g. [30,45]), as they do not allow for the upstream propagation of disturbances past the inflow plane. A relaxation of the inlet boundary condition, on the other hand, requires certain ad hoc adjustments along the lateral boundary, in order to keep the breakdown within the computational domain. This, in turn, has the disadvantage of affecting the initiation and mode selection of the vortex breakdown, cf. Althaus et al. [2]. Snyder and Spall [42] investigate the possible influence that upstream propagating waves might have on the breakdown structure of trailing wing vortices. To this end, they simulate breakdown in a tube-and-vane apparatus. They compare results obtained from a simulation of the full apparatus with results considering fixed inlet conditions, derived from the results using the complete vane geometry. These calculations reveal that breakdown location and structure are essentially unaffected by the use of fixed, steady inflow conditions. This suggests that our choice of fixed, steady inflow boundary conditions will not unduly constrain the development of the various vortex breakdown modes further downstream.

4.1.1. Grabowski profile

In order to study the case of low entrainment, we focus on a class of profiles that were already investigated by Grabowski and Berger [20] in steady, axisymmetric simulations. This provides an opportunity to validate our own axisymmetric steady state results, and to study both the unsteady evolution as well as three-dimensional effects for this class of flows, referred to as 'Grabowski profiles' hereafter. The non-dimensional form of the velocity profile is obtained by scaling the radius with the characteristic core radius $L = R$, and the velocities with the freestream axial velocity $U = \tilde{v}_{z,\infty}$. The two-parameter non-dimensional velocity components then take the form

$$\begin{aligned} &v_\theta(0 \leqslant r \leqslant 1) = Sr(2 - r^2),\\ &v_\theta(1 \leqslant r) = S/r,\\ &v_r(r) = 0,\\ &v_z(0 \leqslant r \leqslant 1) = \alpha + (1-\alpha)r^2(6 - 8r + 3r^2),\\ &v_z(1 \leqslant r) = 1. \end{aligned} \tag{11}$$

Here the swirl parameter S represents the azimuthal velocity at the edge of the core, $S = \tilde{v}_\theta(R)/\tilde{v}_{z,\infty}$. The coflow parameter α denotes the ratio of the velocity at the axis to the free

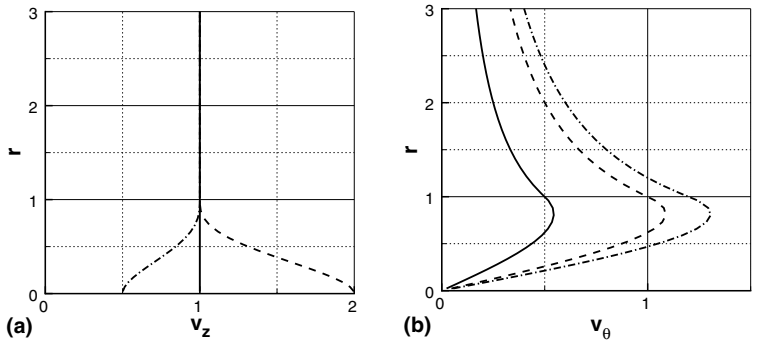

Fig. 3. (a) Axial velocity distribution for the Grabowski profiles: solid line $\alpha = 1.0$, dashed line $\alpha = 2.0$, dash-dot line $\alpha = 0.5$. (b) Azimuthal velocity distribution for the Grabowski profiles: solid line $S = 0.5$, dashed line $S = 1.0$, dash-dot line $S = 1.2$.

stream velocity, $\alpha = \tilde{v}_{z,c}/\tilde{v}_{z,\infty}$. Setting α greater or less than one yields the jet- or wake-like behavior, respectively. The properties of the Grabowski profile are sketched in Fig. 3.

4.1.2. Maxworthy profile

The second class of profiles is intended to model the high entrainment, top-hat jet flows studied in the experiments of Billant et al. [7] and Maxworthy (private communication). To render the velocity components dimensionless, length and velocity are scaled by the core radius $L = R$ and the centerline velocity $U = \tilde{v}_{z,c}$, respectively. This yields the dimensionless velocity profiles of the form

$$\begin{aligned} v_\theta(r) &= \frac{Sr}{2}\left[1 - \operatorname{erf}\left(\frac{r-1}{\delta}\right)\right], \\ v_r(r) &= 0, \\ v_z(r) &= 1 - \frac{\alpha - 1}{2\alpha}\left[1 + \operatorname{erf}\left(\frac{r-1}{\delta}\right)\right]. \end{aligned} \tag{12}$$

Hence we obtain a three-parameter velocity profile defined by the swirl parameter S, the dimensionless shear-layer thickness δ, and the coflow parameter α. The latter is defined in the same way as for the Grabowski profile ($\alpha = \tilde{v}_{z,c}/\tilde{v}_{z,\infty}$), while $S = \Omega_c \tilde{r}/\tilde{v}_{z,c}$ approximates the solid body rotation at the axis Ω_c for sufficiently small $\delta \lessapprox 0.2$. This type of profile will be referred to as the 'Maxworthy profile' hereafter. Its properties are sketched in Fig. 4.

4.2. Outflow boundary

The present investigation is designed to simulate the non-linear temporal and spatial development of swirling flows. This precludes the use of any periodicity assumptions to reduce the computational domain. In particular, the simple periodic outflow boundary conditions successfully employed by Brancher et al. [9] and Hu et al. [24] in simulations of temporally growing flows can not be applied. In agreement with the observations by Jin and Braza [25] for plane shear-layer

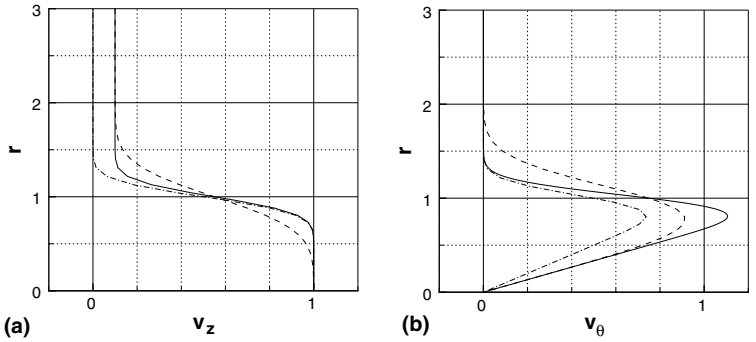

Fig. 4. (a) Axial velocity distribution for the Maxworthy profile: solid line $\delta = 0.2$, $\alpha = 10$, dashed line $\delta = 0.4$, $\alpha = 10$, dash-dot line $\delta = 0.2$, $\alpha = \infty$. (b) Azimuthal velocity distribution for the Maxworthy profile: solid line $S = 1.5$, $\delta = 0.2$, dashed line $S = 1.5$, $\delta = 0.4$, dash-dot line $S = 1.0$, $\delta = 0.2$.

simulations, Neumann type boundary conditions were found to yield non-physical feedback, which strongly affects the global stability of the flowfield, cf. Buell and Huerre [13]. Hence we choose to follow Orlanski [34] and apply convective boundary conditions for each velocity flux component

$$\frac{\partial q_i}{\partial t} + C\frac{\partial q_i}{\partial z} = 0. \tag{13}$$

This boundary condition, also known as non-reflective, radiation, absorbing, or advective condition, is spatially and temporally local, and thus computationally very efficient to implement. In contrast to Orlanski, however, C is taken to be a constant convection velocity of the large-scale structures, rather than a local propagation velocity. It has to be determined experimentally or in preliminary runs. Obviously it is important to show that the value of C is not critical to the solution in the interior of the domain. This is demonstrated by, among others, Salvetti et al. [41] for coaxial jets and by Pauley et al. [35] for two-dimensional separating laminar boundary layers. For the present case of swirling jets, it will be shown in Section 5. While a constant value of C yields satisfactory results for incompressible flows, there are efforts to determine an optimal C-value to ensure non-reflecting behavior in compressible and aeroacoustics computations, cf. e.g. Colonius [16] and Rowley and Colonius [39].

For all of the above examples, the vortical structures generated in the interior of the domain are convected across the boundary without any significant distortion or reflection. Nevertheless, Akselvoll and Moin [1] observe that this boundary condition does have an upstream influence over about one dimensionless length. Salvetti et al. [41] point out that within this zone the streamlines are artificially forced to be perpendicular to the boundary. We suggest that this may be a result of the one-dimensional origin of this boundary condition. Thus, in the results presented in Section 5, this zone near the outflow boundary should be considered from this perspective.

Finally we wish to address the question whether the in- and outflow boundary conditions agree with the implicit assumptions necessary to solve the Poisson equation (8) by a cosine expansion for ϕ in the axial direction. Verzicco and Orlandi [47] show that $\hat{q}_i = q_i^{l+1} + O(\Delta t^2)$. Consequently we take $\hat{q}_i = q_i^{l+1}$ on the domain boundary without loss of accuracy which, with Eq. (7), yields

$G_i\Phi = 0$. The proof for the in- and outflow condition is now straightforward, considering that the convective condition (13) is determined at time levels l and $l-1$, in line with the convective terms H_i.

4.3. Radial boundary

Earlier three-dimensional simulations initiated vortex breakdown by prescribing a more or less artificial pressure gradient, which was generated by specifying the axial velocity on the radial boundary. Subsequently it was demonstrated that the selection of this pressure gradient determines the breakdown mode, cf. Althaus et al. [2] and Spall and Snyder [46]. The present simulations seek to eliminate this dependency, by specifying a radial boundary condition that is nearly transparent to the flow. In the following, we discuss several possible approaches in this regard, for which results will be discussed is Section 5.

4.3.1. Free-slip condition

If the coflow is sufficiently large, free-slip conditions can be applied similarly to incompressible shear-layer simulations (e.g. [28,41]). Generally, free-slip conditions are defined by vanishing tangential viscous stress components on the cylindrical streamsurface. Thus the non-dimensional free-slip conditions in the present notation read

$$q_r = 0, \quad \frac{\partial q_\theta}{\partial r} - \frac{q_\theta}{R_d} = 0 \quad \text{and} \quad \frac{\partial q_z}{\partial r} = 0. \tag{14}$$

Note that the above is true for axisymmetric and three-dimensional cases alike. In the present investigation we neglect the expression q_θ/R_d above. This is justified by the fact that for large R_d this term decreases like $1/R_d^2$ for the Grabowski profile. For the Maxworthy profile, it is even smaller. In addition, possible additional errors introduced by this simplification are far removed from the dominant dynamic regions of the flow, so that they have a negligible influence. Further, similarly to the inflow condition, the free-slip condition satisfies the implicit requirement $\partial\phi/\partial r = 0$ necessary for the solution of the Poisson equation (8).

Assuming impermeable lateral boundaries Gresho [22] shows for a two-dimensional Cartesian coordinate system that any constant C automatically satisfies global mass conservation. This favorable property can also be shown to hold for an axisymmetric case if impulsive starts (as defined by Gresho) are precluded.

4.3.2. Neumann condition

If appreciable entrainment occurs, such as for the top-hat jet profile, the free-slip boundary condition requires unpractically large radial dimensions of the computational domain in order to avoid feedback from the boundaries. In order to be able to truncate the domain at smaller radii, one has to allow for mass and momentum to be exchanged across the radial boundary. One possibility in this regard is to take the homogeneous Neumann condition for the radial flux component

$$\frac{\partial q_r}{\partial r} = 0. \tag{15}$$

This implies constant radial mass flux through concentric cylindrical shells, which models entrainment at large radii. As stated by Kourta et al. [28], the most challenging problem in employing the homogeneous Neumann boundary condition is to globally conserve mass. This is due to the absence of a time derivative in the incompressible continuity equation; a feature that is retained in the fractional-step formulation. On the other hand, it is much more straightforward to conserve mass globally in the artificial compressibility method [14] for steady flows, and its dual-time stepping extension for unsteady flows. However, this approach is computationally much less efficient than the fractional-step method employed here.

In two-dimensional plane mixing layer simulations, Kourta et al. [28] are unable to conserve global mass for long simulation times when they use the homogeneous Neumann condition at the lateral boundaries in combination with a boundary layer type outflow condition. On the other hand, our convective outflow boundary condition introduces the free parameter C, which can be used to enforce global mass conservation, as will be explained below.

In order to study the interaction between an open radial boundary employing Eq. (15) and a prescribed convective outflow condition, we consider two combinations of Dirichlet/Neumann conditions at the radial boundary. The first one represents the straightforward extension of the free-slip condition, i.e. $\partial q_\theta/\partial r = \partial q_z/\partial r = 0$ (*type 1*). However, the condition $\partial q_\theta/\partial r = 0$ is only approximately satisfied for velocity profiles decreasing like $1/R_d^2$. This leads to the second version, in which q_θ is prescribed in a Dirichlet fashion by setting it to its value at the inflow $z = 0$, i.e. $q_\theta = q_\theta(R_d, 0)$. Further we prescribe the axial velocity component in a Dirichlet fashion, i.e. $q_z = q_z(R_d, 0)$ (*type 2*). In both versions mass is conserved by slightly modifying the axial velocity component at the outflow boundary $z = Z_d$. This is done in the form

$$q_z(\theta, r, Z_d) = q_z^*(\theta, r, Z_d) + \Delta\dot{V} \cdot \frac{W(r)}{\int W(r)\,\mathrm{d}A_\circ}, \tag{16}$$

where q_z is the axial velocity component conserving global mass, and q_z^* is the one obtained from applying the simple radiation condition (Eq. (13)) at the outflow. $\Delta\dot{V} = \int (q_z(0) - q_z(Z_d))\,\mathrm{d}A_\circ - \int q_r(R_d)\,\mathrm{d}A_\square$ is the volume flux necessary to conserve global mass. Here $\int (q_z(0) - q_z(Z_d))\,\mathrm{d}A_\circ$ and $\int q_r(R_d)\,\mathrm{d}A_\square$ represent the difference between axial in- and outflow, and radial entrainment, respectively. The infinitesimal areas are defined in the common way, i.e. $\mathrm{d}A_\circ = r\,\mathrm{d}\theta\,\mathrm{d}r$ and $\mathrm{d}A_\square = R_d\,\mathrm{d}\theta\,\mathrm{d}z$. $W(r)$ denotes the weight function governing the distribution of the necessary axial velocity adjustments at the outflow. Typically we take $W(r) = 1 - (r/R_d)^2$. Since this modification causes slight variations of C in the radiation condition, it has to be demonstrated that the solution is not influenced by the choice of $W(r)$. This will be shown in Section 5. A significant disadvantage of this procedure is that in order to retain the global mass conservation with $\hat{q}_r = q_r^{l+1}$, i.e. $\partial\phi/\partial r = 0$ on the radial boundary, q_r has to be known a priori. This renders the calculations employing $\partial q_r/\partial r = 0$ iterative, and therefore computationally less efficient.

Boersma et al. [8], investigating the spatio-temporal evolution of an incompressible jet without swirl, apply a so-called traction-free condition at the lateral boundary. They find that the main advantage of the traction-free condition over a free-slip condition is that velocity across the boundary is allowed. This important property is retained in the simpler Neumann conditions presented above. Further they find that the traction-free boundary condition is numerically stable only below a certain cell Reynolds number. Since swirling flows typically entrain more mass than non-swirling jets and the application of a radial grid stretching in the present scheme we expect

numerical stability problems, similar to those experienced by Boersma et al. [8] at the outflow for turbulent flow. Thus the numerical scheme potentially has to be stabilized in the spirit employed here for the Neumann conditions, rendering it iterative, and therefore computationally less efficient.

4.3.3. Radiation condition

The lower computational efficiency caused by employing the homogeneous Neumann condition in the radial direction renders the time-explicit formulation of an open radial boundary condition attractive. Since swirling flow fields exhibit qualitatively wave-like features ([6,31,33], etc.), the boundary conditions should simulate the propagation of waves out of the computational domain; that is to say, they should allow the motion of outgoing flow to pass through the boundary without being reflected, while incoming wave amplitudes should have no effect on the solution inside the domain and hence be set to 0.

However, a detailed derivation of such radiative boundary conditions starting from the wave equation in polar coordinates [17,19] is not pursued here, since no matching with the Navier–Stokes equations in a mathematically exact way is possible, cf. Jin and Braza [25]. Instead we take the condition

$$\frac{\partial q_i}{\partial t} + C_r \frac{\partial q_i}{\partial r} = 0, \tag{17}$$

at the radial boundary in the spirit of the employed outflow condition, thus implicitly requiring $\partial\phi/\partial r = 0$. Here C_r represents the convection velocity in the radial direction and $C_r > 0$ guarantees the properties discussed above. In Section 5 it will be shown that, similarly to the outflow boundary, the exact value of C_r is not critical for the simulation.

In the following, we will demonstrate that simulations with open convective radial and downstream boundaries automatically conserve global mass if $C_r = \text{const.}$ and $C = \text{const.}$ Following Gresho [22] the problem has to be well posed for $t \geqslant 0$, and impulsive starts have to be excluded. Integration of the boundary conditions (Eqs. (13) and (17)) over time and the surface of the domain yields

$$\int_{A_\circ} \int_0^t C \frac{\partial q_z}{\partial z} \mathrm{d}t \, \mathrm{d}A_\circ + \int_{A_\square} \int_0^t C_r \left(\frac{\partial q_r}{\partial r} \right) \mathrm{d}t \, \mathrm{d}A_\square = 0, \tag{18}$$

where the first (second) term has to be evaluated at the outflow boundary $z = Z_d$ (radial boundary $r = R_d$). Note that the derivation of the above expression requires global mass conservation at every instant $t \geqslant 0$, which removes the time derivatives in the boundary conditions. The above equation can be simplified further if axisymmetry is assumed. Under this condition, and by employing the continuity equation (1), the surface integrals can be reduced to an evaluation of velocity components on the boundaries

$$\int_0^t \left(\frac{C}{C_r R_d^2} q_r(R_d, Z_d) + q_z(R_d, Z_d) - q_z(R_d, 0) \right) \mathrm{d}t = 0. \tag{19}$$

Hence Eq. (17) together with the convective outflow boundary condition (13), satisfies global mass conservation of an axisymmetric calculation automatically if $q_r(R_d, Z_d) = 0$ and $q_z(R_d, Z_d) = q_z(R_d, 0)$.

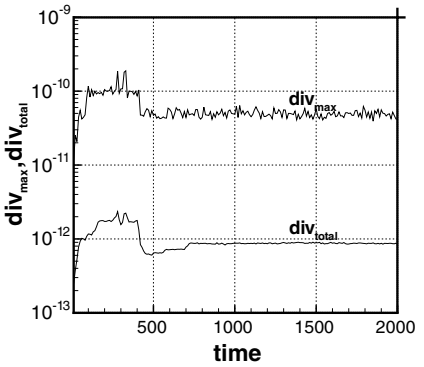

Fig. 5. Global (div_{total}) and maximal local (div_{max}) divergence as function of time. The considered three-dimensional Grabowski case employs $Re = 200$, $S = 1.095$ and $\alpha = 1.0$.

Numerical simulations of three-dimensional cases performed during the present investigation show that for sufficiently far removed radial boundaries, azimuthal variations along them can be neglected. Fig. 5 depicts the global (div_{total}) mass conservation, as well as the maximum local divergence (div_{max}), for a three-dimensional simulation of a Grabowski profile with $S = 1.095$ and $\alpha = 1$ at the Reynolds number $Re = 200$. Both of these divergence diagnostics remain near machine accuracy. This flow will be discussed in greater detail below.

5. Numerical results

We shall base our discussion of the main results on two representative reference cases; one for the Grabowski profile and one for the Maxworthy profile. Unless specified otherwise, the reference cases employ physical and numerical parameters as follows: while the Reynolds number is uniformly set to $Re = 200$, we take for the Grabowski profile $S = 1.095$ and $\alpha = 1.0$, and for the Maxworthy profile $S = 1.5$, $\delta = 0.2$ and $\alpha = 100.0$. All simulations start from an initial condition that assumes a cylindrical flow with a velocity profile determined by the above parameters. Occasionally, we refer to the 'steady state' of a simulation. By this we mean that the velocity components change by less than 10^{-6} over $\Delta t = 10$.

The computational domain for both cases typically has the dimensions $R_d = 10$ and $Z_d = 20$. Note that $R_d = 10$ represents the minimum requirement for the optimal radial boundary conditions in order to obtain solutions independent of numerical parameters. Other boundary conditions may require substantially larger domains, as will be discussed below. The reference case is resolved by $n_r = 61$ ($n_R = 17$) grid points clustered around the axis and $n_z = 193$ equidistant grid points in the axial direction. In the non-axisymmetric simulations $n_\theta = 61$ grid points are taken in the azimuthal direction. The time step employed is typically $\Delta t = 0.025$.

The grid independency has been checked by comparing the reference case (solid lines) with a high resolution simulation (dashed lines) employing $n_r = 97$, $n_z = 241$ and $n_\theta = 97$ grid points, cf. Fig. 6 for the example q_θ at $z = 5$ and $r = 1$. The constant horizontal lines, corresponding to axisymmetric calculations, reveal a marginal difference of about 0.2%, with respect to the high

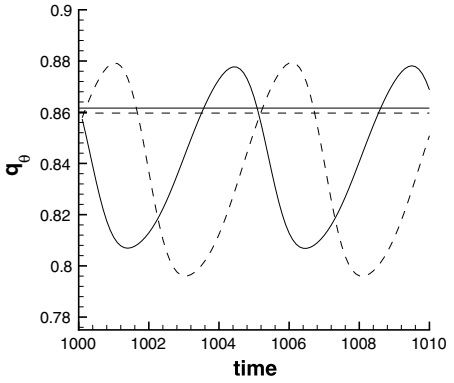

Fig. 6. Azimuthal velocity component q_θ of the reference (solid line) and higher resolution case (dashed line) over time for the radiation condition. The constant horizontal lines, corresponding to axisymmetric calculations, reveal a marginal difference of about 0.2%. The oscillatory behavior of the three-dimensional simulations exhibits no detectable difference in the period, however the maxima and minima differ by 0.2% and 1.4%, respectively.

resolution case. The oscillatory behavior of the three-dimensional simulations exhibits no detectable difference in the period, however the maxima and minima differ by 0.2% and 1.4%, respectively. The phase shift between the computations is caused by grid dependent round-off errors feeding on a physical instability, which ultimately yields the oscillatory behavior of the flow field. As additional accuracy check for the axisymmetric steady state solutions we shall compare with the vortex breakdown results of Grabowski and Berger [20] throughout this section.

The convective velocity for the outflow is set to $C = 0.6$. In order to establish that the numerical solution is independent of the value of C, we conducted simulations for $0.01 \leqslant C \leqslant 1.1$. Quantitative comparisons showed maximum deviations in $|\Delta q_i|$ and $|\Delta p|$ of order 10^{-5} at the boundaries, and even smaller in the interior of the domain.

In the following, we will discuss the results obtained with the various boundary conditions introduced in Section 4 for both reference cases in detail. Their main properties are summarized in Table 1.

5.1. Grabowski profile

As a typical low entrainment case, we consider the Grabowski reference profile. For the axisymmetric steady state, we can compare our results directly with the simulations of Grabowski and Berger [20]. For this purpose, we follow these authors and present streamline plots projected

Table 1
Overview of the discussed lateral boundary conditions

Lateral boundary condition	Global mass conservation	Numerical efficiency
Free slip	Automatic	Explicit
Neumann (1)	Weight function	Iterative
Neumann (2)	Weight function	Iterative
Radiation	Automatic	Explicit

onto a meridional plane, cf. Fig. 7. The present results obtained with a free-slip or simple radiation condition at the radial boundary display good qualitative agreement with Grabowski and Berger's original work, although their simulation is not as well resolved spatially. A quantitative comparison between the present results with the above two boundary conditions yields maximum differences on the order of 10^{-3} for $|\Delta q_i|$ and $|\Delta p|$. A variation of the numerical parameter C_r ($C_r = 0.1$ for the simulation shown) in the range $0.01 \leqslant C_r \leqslant 1.1$ results in a maximum difference of 10^{-7} for these quantities.

In order to determine which of the above radial boundary conditions allows for the smallest control volume, we compare results for a domain size of $R_d = 2$, cf. Fig. 7(d). Although the radial boundary clearly affects the solution in both cases, the free-slip condition alters the bubble much more dramatically, by forcing the streamlines to be parallel to the radial boundary. In contrast, the radiation condition produces a somewhat larger bubble that nonetheless resembles the one obtained for the larger domain $R_d = 10$ significantly better.

As an example of a more detailed validation with Grabowski and Berger's [20] results, Fig. 8 displays the axial velocity component along the axis for the present reference case (a), along with their original results (b). Note that due to the staggered grid q_z is not evaluated directly on the axis ($r = 0$) so that the data shown are taken at the radial position closest to the axis. Both radial boundary conditions deliver nearly indistinguishable results, which agree well with the classic work.

In order to determine the effect of different radial boundary conditions on the temporal development of the axisymmetric flow, we consider time traces of velocity components at several positions throughout the computational domain. Fig. 9 shows such data for the axial velocity

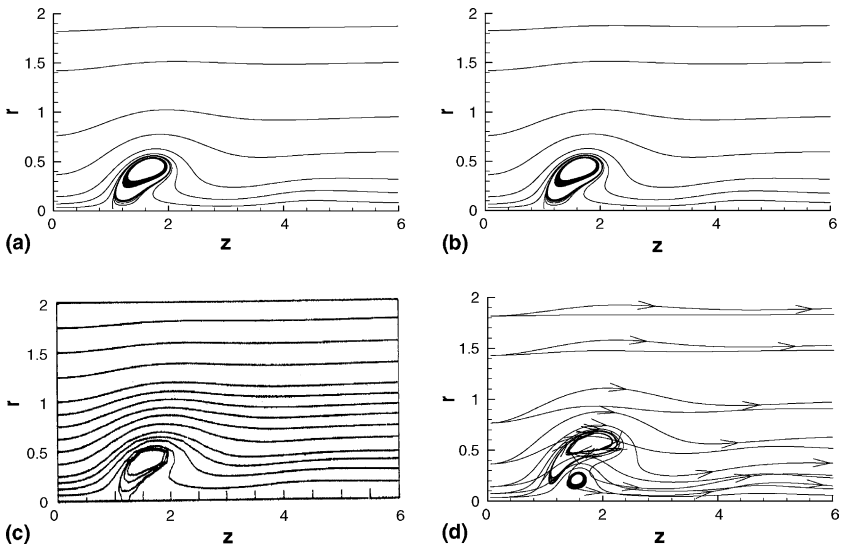

Fig. 7. Streamlines of the Grabowski reference case at steady state. Comparison of the free-slip (a) and the radiation condition with $C_r = 0.1$ employed at $R_d = 10$ (b). The original streamlines obtained by Grabowski and Berger [20] (reprinted with the permission of Cambridge University Press) are shown in (c). Finally, (d) displays streamlines obtained with the free-slip (no arrows) and radiation condition ($C_r = 0.1$, arrows) applied at $R_d = 2$.

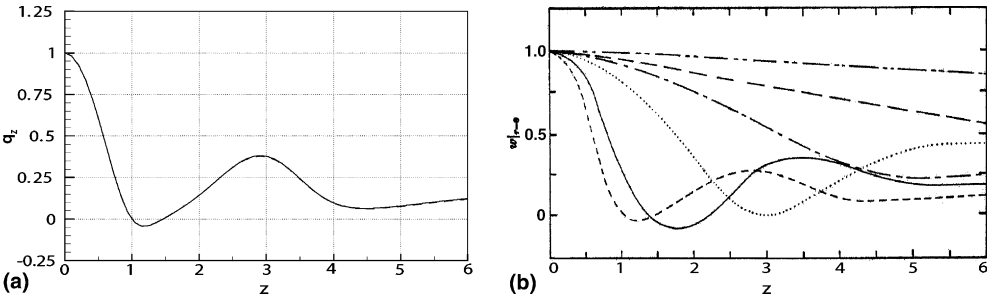

Fig. 8. Axial velocity component closest to the axis. (a) Present simulation: the solid and dashed lines represent the free-slip and simple radiation ($C_r = 0.1$) condition, respectively. (b) Simulation of Grabowski and Berger [20] (reprinted with the permission of Cambridge University Press): the dashed line applies to the swirl parameter value $S = 1.095$ employed in the present simulations.

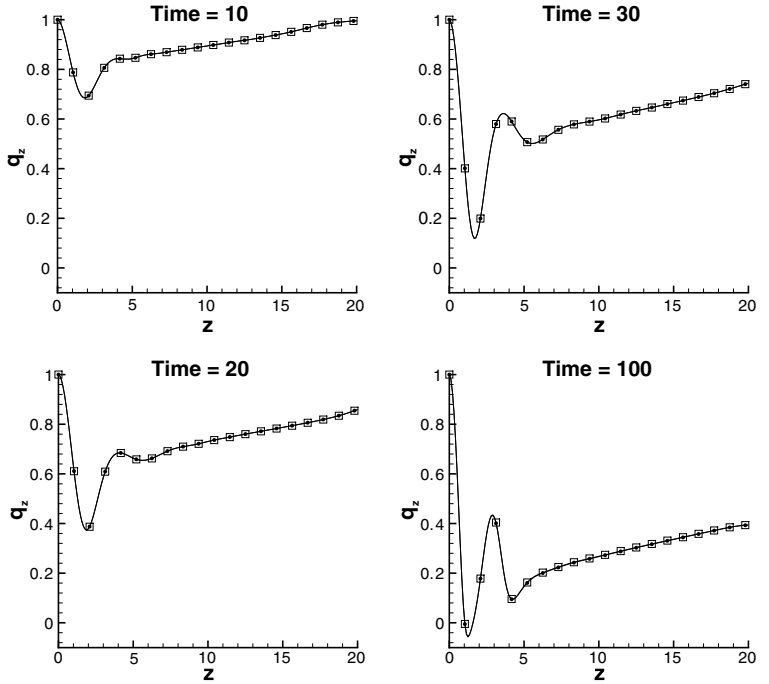

Fig. 9. Temporal evolution of the axisymmetric Grabowski reference case, obtained with free-slip (open squares) and simple radiation (filled circles) boundary conditions.

component closest to the axis. No discernible differences are observed between the free-slip (open squares) and simple radiation (filled circles) lateral boundary conditions.

Correspondingly similar behavior is also observed for three-dimensional simulations of the reference case. Fig. 10 displays streaklines at times $t = 50$ and 750 obtained with the simple radiation condition. A transition from a quasi-steady axisymmetric bubble breakdown state to a

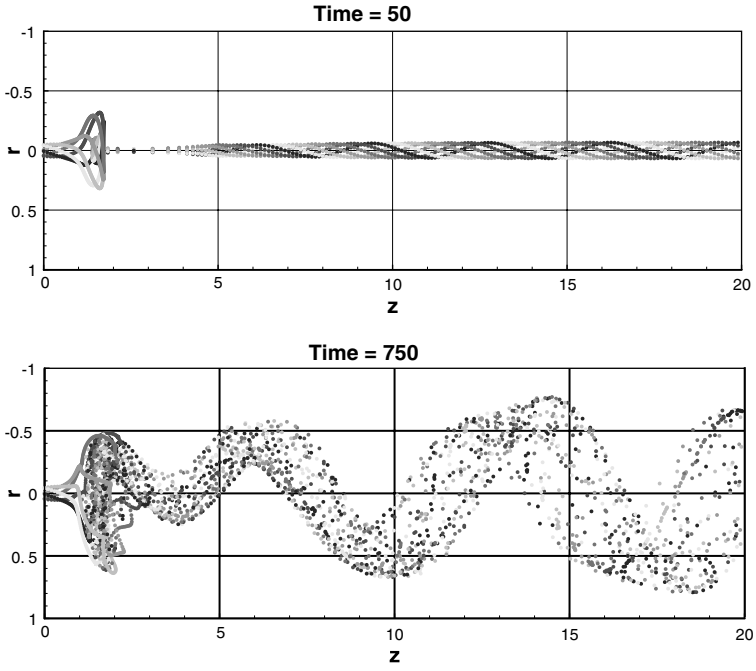

Fig. 10. Streaklines for the three-dimensional simulation of the Grabowski reference case with $S = 1.095$. Shown here is the dynamical evolution obtained with the radiation boundary condition ($C_r = 0.1$). Essentially identical results are obtained for the free-slip condition.

helical type is observed. The same transition occurs, at the same time, with the free-slip boundary condition.

If the swirl is increased to $S = 1.3$, with all other physical and numerical parameters left unchanged, a double-helical breakdown mode emerges from a quasi-steady axisymmetric bubble state (Fig. 11). These highly unsteady, three-dimensional results obtained with a fixed inflow profile are quite similar to the simulation data presented by Breuer and Hänel [11], Breuer et al. [12] and Spall and Gatski [43] for lateral pressure-based boundary conditions.

The application of any of the homogeneous Neumann conditions discussed above at the radial boundary is found to require a computational domain larger than $Z_d = 20$ and $R_d = 10$, in order

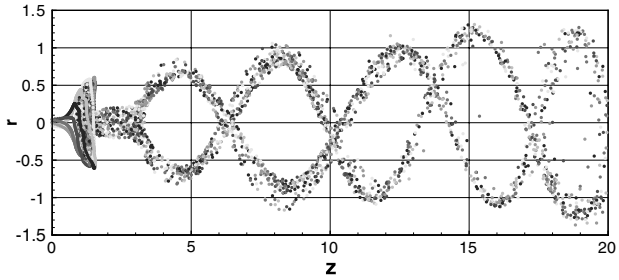

Fig. 11. Double-helical breakdown type as observed for the Grabowski reference case with higher swirl $S = 1.3$.

to render results independent of the weight function W. Since, as shown above, free-slip and radiation conditions yield satisfactory results for smaller domains, we thus do not pursue homogeneous Neumann conditions any farther here.

5.2. Maxworthy profile

In contrast to the low entrainment case, the lateral boundary for a high entrainment case generally does not approximate a stream surface, unless it is positioned at very large radial distances. To avoid the additional computational effort associated with such a large domain, it is advantageous to allow for mass and momentum transport across the boundary. This issue is clearly demonstrated in Fig. 12, which presents results for the axisymmetric, steady state Maxworthy profile.

Fig. 12(a) demonstrates that a free-slip boundary condition applied at the reference position $R_d = 10$ produces an unphysical recirculation region near the outflow boundary. Increasing the radial dimension of the computational domain to $R_d = 16$ eliminates this undesirable behavior, at the expense of additional grid points. A similar behavior, even though less pronounced, can be seen for the homogeneous Neumann condition type 2. Application of the radiation (b) or the homogeneous Neumann condition (type 1) (c) yields flow fields that deliver almost indistinguishable results in both domains $R_d = 10$ and 16. It should be kept in mind that in the far field the velocity values are so small that even minute changes can significantly alter the streamline shapes. The maximum differences $|\Delta q_i|$ and $|\Delta p|$ for cases (b and c) are less than 1% of the velocity

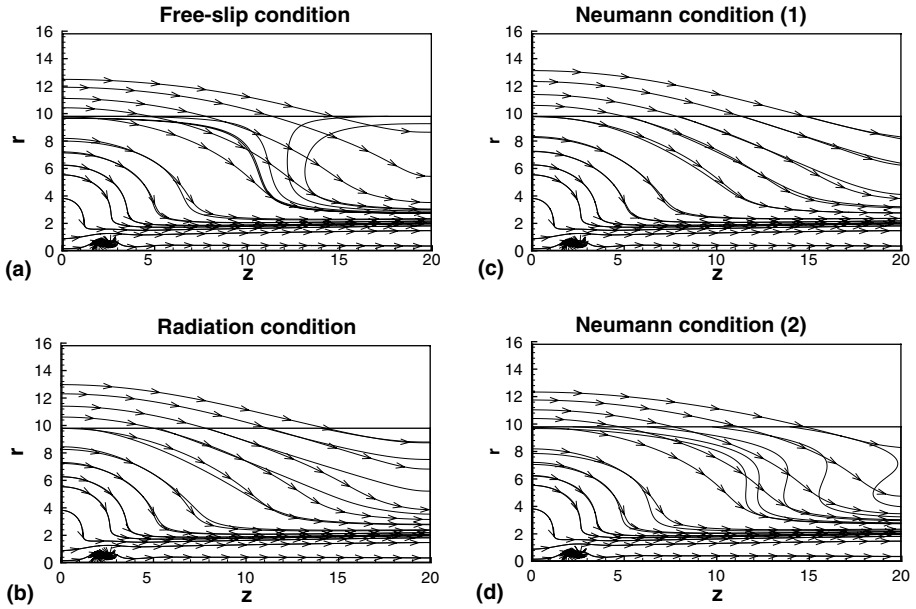

Fig. 12. Streamlines obtained for the Maxworthy reference case, for different radial boundary conditions at the radial positions $R_d = 10$ (reference case, no arrows) and $R_d = 16$ (arrows); (a) free-slip condition, (b) radiation condition, (c,d) Neumann condition (type 1,2), respectively.

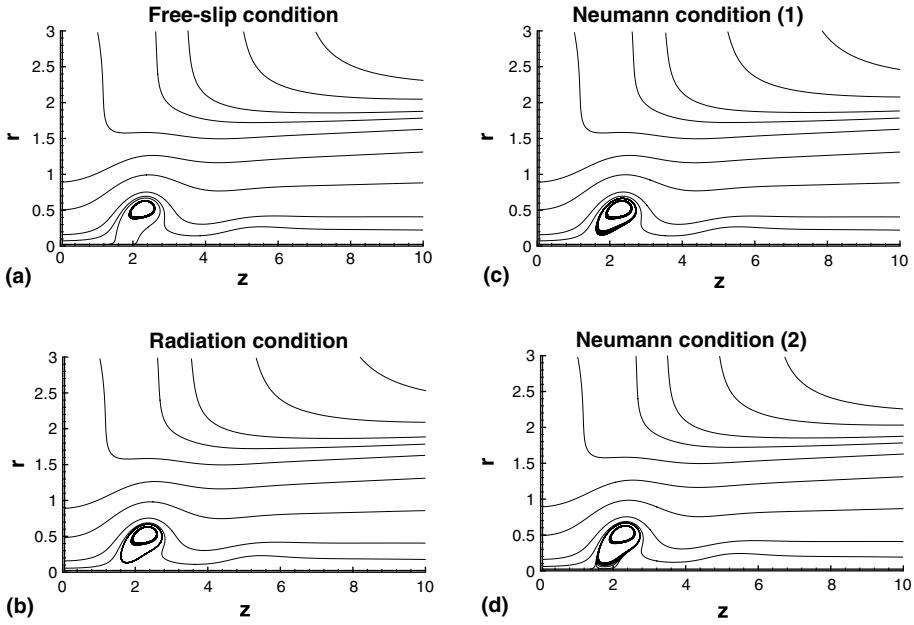

Fig. 13. Streamlines of the Maxworthy reference case at steady state for different radial boundary conditions at $R_d = 10$: (a) free-slip condition, (b) radiation condition with $C_r = 0.1$, (c) homogeneous Neumann condition type 1, (d) type 2.

scale. A more detailed look at the near field at $R_d = 10$ is provided in Fig. 13. All boundary conditions yield qualitatively nearly indistinguishable results, with the largest deviation exhibited by the free-slip and Neumann type 2 condition.

We wish to point out that increasing the swirl parameter to $S = 1.7$, with all other parameters left constant, gives rise to a two-celled bubble structure (Fig. 14). This result is similar to the numerical simulation data of Breuer and Hänel [11] and Spall et al. [44], and it indicates that the fixed inflow conditions employed in the present investigation do not prevent the existence of two-celled structures, as has been suspected by Spall et al., among others.

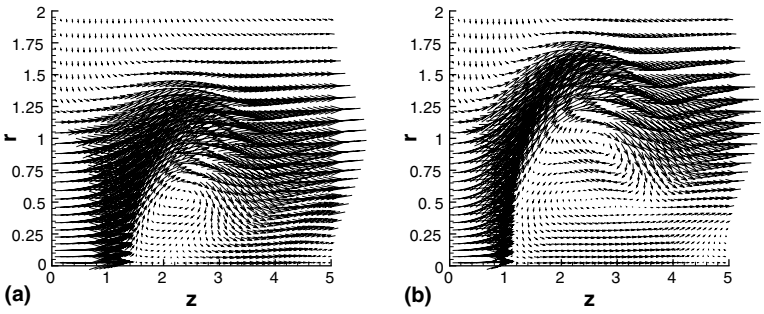

Fig. 14. Projected velocity vectors for the reference Maxworthy case $S = 1.5$ (a) and higher swirl $S = 1.7$ (b) at steady state. The low swirl bubble exhibits one vortex ring, while the higher swirl gives rise to two vortex rings, i.e. a two-celled structure.

5.3. Mass conservation

As seen above, the use of different boundary conditions can lead to quantitative changes in the flow field. In part, this is due to the distinct ways in which global mass is conserved for each of the boundary conditions. The free-slip condition requires the radial flux to be 0 ($q_r = 0$) over the whole axial extent of the radial boundary (Fig. 5a). Thus, the requirement $q_r(R_d, Z_d) = 0$ for global mass conservation (cf. Section 4) imposed by the outflow condition is satisfied trivially, while the free-slip condition on the radial boundary allows $q_z(R_d, Z_d)$ to adjust freely. This is shown in the right detail insert in Fig. 15(c), which demonstrates that $q_z(R_d, Z_d) \neq q_z(R_d, 0) = 1.0$.

The simple radiation condition enforces global mass conservation by means of additional constraints on the velocity components at the boundaries, cf. Section 4.3.3. Applying it at the

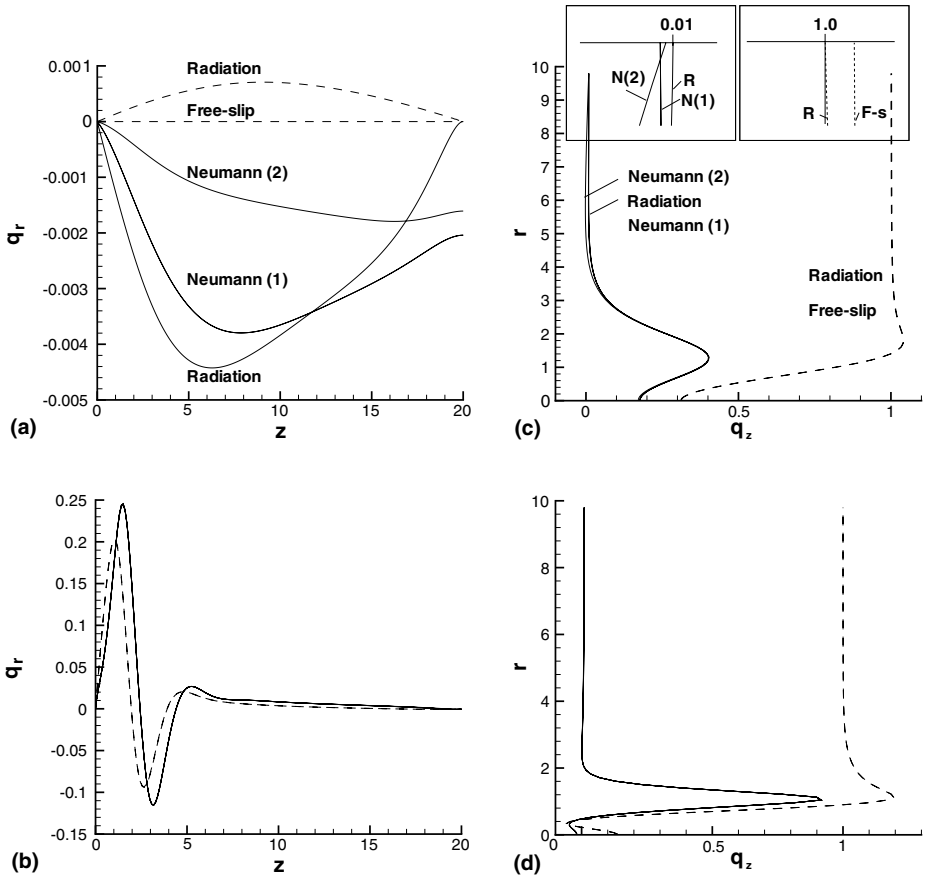

Fig. 15. Velocity components normal to the radial and outflow boundaries, respectively, obtained with different boundary conditions, for the Grabowski (dashed lines) and Maxworthy reference cases (solid lines). Radial flux component q_r at the radial boundary (a) and radius $r = 1$ (b). Axial velocity component q_z at outflow boundary (c) and axial position $z = 2$ (d). The insert in (c) demonstrates that the radiation boundary condition requires $q_z(R_d, Z_d) = q_z(R_d, 0)$. All cases are displayed in all frames. If only one line is visible, this indicates a collapse of the results for different boundary conditions.

radial boundary requires $q_z(R_d, Z_d) = q_z(R_d, 0)$, cf. the detail inserts of Fig. 15(c). On the other hand, applying the radiation condition at the outflow boundary requires $q_r(R_d, Z_d) = 0$ in order to satisfy global mass.

Both types of the homogeneous Neumann boundary condition conserve global mass through modifying the outflow boundary condition by means of the weight function W. This removes the limitations concerning $q_z(R_d, Z_d)$ and $q_r(R_d, Z_d)$. While the resulting normal velocity profiles at the boundary have qualitatively different shapes, the quantitative differences are well below one percent of the characteristic velocity. They produce essentially indistinguishable velocity distributions in the interior of the domain, cf. Fig. 15(b) and (d).

In particular we wish to point out that the application of a Neumann condition which differs from type 1 only by employing $q_\theta(R_d) = q_\theta(R_d, 0)$ instead of $\partial q_\theta(R_d)/\partial r = 0$ exhibits indistinguishable results from type 1, even at the boundaries.

The results obtained with the homogeneous Neumann boundary conditions are insensitive to the particular choice of the weight function W. This has been confirmed for the Maxworthy reference case by a qualitative comparison of the streamlines obtained for the weight functions $W(r) = 1 - (r/R_d)^2$, $W(r) = 1$ and $W(r) = (r/R_d)^2$. A quantitative comparison of each of these cases with a reference case that employs the radiation boundary condition exhibits maximum values of $|\Delta q_i|$ and $|\Delta p|$ on the order 10^{-3}.

Fig. 16 discusses the quality of mass conservation for both reference cases by means of the maximum local divergence in the flow field as function of time. For the Grabowski profile (Fig. 16a) the dashed line represents a case with radiation boundary condition, while the solid line represents corresponding data for the free-slip condition. It is demonstrated that the local divergence values are comparable for the free-slip and the simple radiation conditions.

The Maxworthy profile is discussed in Fig. 16(b). Here the radiation boundary condition is represented by the solid line, exhibiting comparable maximum local divergence values with the Grabowski case. Application of the homogeneous Neumann condition without enforcing global mass conservation leads to a dramatic increase of local divergence values (dashed line) in time,

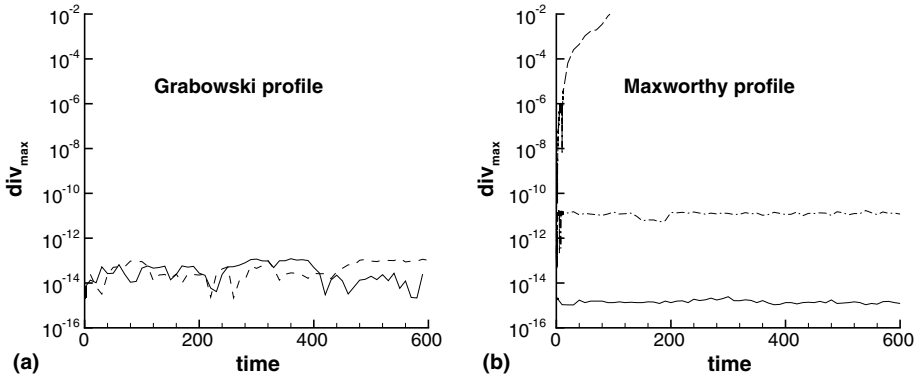

Fig. 16. Mass conservation for both reference cases, with different boundary conditions. (a) Grabowski reference case with free-slip (solid line) and radiation boundary condition (dashed line). (b) Maxworthy reference case with radiation boundary condition (solid line), and with homogeneous Neumann condition type 1, with and without enforcing global mass conservation (dash-dotted line and dashed line, respectively).

while enforcing it keeps the maximum divergence around machine accuracy (dash-dotted line). The figure shows that the maximum divergence in simulations employing the radiation boundary condition is well below those using the Neumann condition. The reasons for this are explained in detail below.

5.4. Numerical efficiency

The design of an efficient numerical scheme generally favors non-iterative algorithms. Towards this end, we combine the pressure correction variant of the fractional-step method with a direct Poisson solver based on trigonometric expansions. The temporal discretization of the radiation conditions (Eqs. (13) and (17)) allows us to maintain the non-iterative character, as it employs an explicit Euler scheme in order to obtain the velocities at the boundaries *before* the factorized momentum equation (Eq. (5)) is solved for each temporal substep. In this way, simulations employing either the free-slip or the radiation condition at the lateral boundary can be carried out in a non-iterative fashion.

In contrast, application of the homogeneous Neumann condition (Eq. (15)) yields an iterative scheme. This is due to the fact that the radial flux $q_r^{l+1}(R_d)$ at the lateral boundary cannot be determined before solving the momentum equation (Eq. (5)). Consequently, it is impossible to determine the required mass flux $\Delta\dot{V}^{l+1}(q_r^{l+1})$ to conserve global mass at the new time level, on the basis of the data at the old time level l. As a result, one initially has to take $\Delta\dot{V}^{l+1}(q_r^{l})$, which generally does not conserve global mass, and iterate on the resulting $q_r^{l+1}(R_d)$ value until global divergence is lower than 10^{-10}. We limit the number of iterations to a maximum of three per temporal substep. Due to this limitation on the number of iterations, the divergence (global as well as local maximum) is typically higher than for radial free-slip or radiation boundary conditions (Fig. 16b).

6. Summary and conclusions

The present article discusses direct numerical simulations of spatially evolving, unsteady swirling laminar jets exhibiting axisymmetric and three-dimensional vortex breakdown phenomena. For realistic inflow profiles leading to both low and high entrainment, the inception and selection of different breakdown modes are observed, independent of the numerical simulation parameters. Towards this end, the incompressible Navier–Stokes equations are solved in cylindrical coordinates with second-order accuracy all the way to the axis. This approach avoids the artificial perturbations in the azimuthal direction that had been encountered in earlier simulations employing Cartesian coordinates. The time discretization is accomplished by means of a generalized fractional-step method for which we discuss the appropriate intermediate velocity boundary condition that is required to maintain the second (first) order accuracy for velocity (pressure) in time.

A particular challenge lies in the formulation of appropriate conditions at the open radial and outflow boundaries, so that the evolution of swirling jets with vortex breakdown in semi-infinite domains can be simulated. Towards this end, various radial boundary conditions were implemented and tested: a free-slip condition, two types of homogeneous Neumann conditions, and a

radiation condition that is similar to the one employed at the outflow boundary. It was shown that global mass is conserved automatically in the free-slip and simple radiation case. In contrast, the Neumann condition requires some iterative modification at the outflow boundary, based on a weight function W, in order to conserve mass. However, the results are insensitive to the specific form of W. While all boundary conditions lead to maximum divergence values around machine accuracy, the homogeneous Neumann conditions result in the largest divergence values, due to a limit on the number of iterations. In addition, their iterative nature reduces the computational efficiency. The homogeneous Neumann (type 1) and the radiation condition yield nearly indistinguishable flow fields for identical radial domain sizes, while the free-slip and type 2 conditions require a larger domain. Taking into account all of the above findings, the straightforward radiation condition emerges as the optimal lateral boundary condition for the high entrainment jet.

For the low entrainment case, the lateral boundary approximates a streamsurface even at fairly small radial distances. Under these circumstances, the free-slip and radiation conditions produce almost indistinguishable results, as long as the radial boundary is placed at a sufficiently large distance. However, the radiation condition approximates the true physical solution even if the radial boundary is as close as two characteristic core radii from the axis, while for this extreme situation the free-slip condition significantly underpredicts the bubble size. Consequently, the radiation condition emerges as the best choice for both high and low entrainment jets.

Acknowledgements

This work was supported in part by the National Science Foundation. The authors acknowledge several helpful discussions with T. Maxworthy, B. Mück, L. Redekopp and R. Verzicco. Furthermore, we thank R. Verzicco for his generosity in providing several subroutines of his code.

References

[1] Akselvoll K, Moin P. Large-eddy simulation of turbulent confined coannular jets. J Fluid Mech 1996;315:387–411.
[2] Althaus W, Brücker C, Weimer M. Breakdown of slender vortices. In: Green S, editor. Fluid vortices. Kluwer Academic Publishers; 1995. p. 373–426.
[3] Arakawa A. Computational design for long-term numerical integration of the equations of fluid motion: two-dimensional incompressible flow, Part I. J Comput Phys 1966;1:119–43.
[4] Armfield S, Street R. The fractional-step method for the Navier–Stokes equations on staggered grids: the accuracy of three variations. J Comput Phys 1999;153:660–5.
[5] Beam R, Warming R. An implicit finite-difference algorithm for hyperbolic systems in conservation-law form. J Comput Phys 1976;22:87–110.
[6] Benjamin T. Theory of the vortex breakdown phenomenon. J Fluid Mech 1962;14:593–629.
[7] Billant P, Chomaz J-M, Huerre P. Experimental study of vortex breakdown in swirling jets. J Fluid Mech 1998;376:183–219.
[8] Boersma B, Brethouwer G, Nieuwstadt F. A numerical investigation on the effect of the inflow conditions on the self-similar region of a round jet. Phys Fluids 1998;10(4):899–909.
[9] Brancher P, Chomaz J-M, Huerre P. Direct numerical simulations of round jets: vortex induction and side jets. Phys Fluids 1994;6(5):1768–74.

[10] Braza M, Chassaing P, Minh H. Numerical study and physical analysis of the pressure and velocity fields in the near wake of a circular cylinder. J Fluid Mech 1986;165:79–130.
[11] Breuer M, Hänel D. A dual time-stepping method for 3-D, viscous, incompressible vortex flows. Comput Fluids 1993;22(4/5):467–84.
[12] Breuer M, Hänel D, Klöker J, Meinke M. Computation of unsteady vortical flows. Comput Fluids 1993;22(2/3):229–37.
[13] Buell J, Huerre P. Inflow/outflow boundary conditions and global dynamics of spatial mixing layers. In: Proc NASA Ames/Stanford Cent Turbul Res, Summer Program CTR-S88, 1988. p. 19–27.
[14] Chorin A. A numerical method for solving incompressible viscous flow problems. J Comput Phys 1967;2:12–26.
[15] Chorin A. On the convergence of discrete approximations to the Navier–Stokes equations. Math Comput 1969;23:341–53.
[16] Colonius T. Numerically nonreflecting boundary and interface conditions for compressible flow and aeroacoustic computations. AIAA J 1997;35(7):1126–33.
[17] Engquist B, Majda A. Absorbing boundary conditions for the numerical simulation of waves. Math Comput 1977;31(139):629–51.
[18] Faler J, Leibovich S. Disrupted states of vortex flow and vortex breakdown. Phys Fluids 1977;20(9):1385–400.
[19] Givoli D. Non-reflecting boundary conditions. J Comput Phys 1991;94:1–29.
[20] Grabowski W, Berger S. Solutions of the Navier–Stokes equations for vortex breakdown. J Fluid Mech 1976;75:525–44.
[21] Grammeltvedt A. A survey of finite-difference schemes for the primitive equations for a barotropic fluid. Mon Weather Rev 1969;97(5):384–404.
[22] Gresho P. Some interesting issues in incompressible fluid dynamics, both in the continuum and in numerical simulation. Adv Appl Mech 1992;28:45–140.
[23] Harlow F, Welch J. Numerical calculation of time-dependent viscous incompressible flow of fluid with free surface. Phys Fluids 1965;8(12):2182–9.
[24] Hu G-H, Sun D-J, Yin X-Y. A numerical study of dynamics of a temporally evolving swirling jet. Phys Fluids 2001;13(4):951–65.
[25] Jin G, Braza M. A nonreflecting boundary condition for incompressible unsteady Navier–Stokes calculations. J Comput Phys 1993;107:239–53.
[26] Kim J, Moin P. Application of a fractional-step method to incompressible Navier–Stokes equations. J Comput Phys 1985;59:308–23.
[27] Kopecky R, Torrance K. Initiation and structure of axisymmetric eddies in a rotating stream. Comput Fluids 1973;1:289–300.
[28] Kourta A, Braza M, Chassaing P, Haminh H. Numerical analysis of a natural and excited two-dimensional mixing layer. AIAA J 1987;25(2):279–86.
[29] Krause E. The solution to the problem of vortex breakdown. In: Morton K, editor. Twelfth International Conference on Numerical Methods in Fluid Dynamics. Lecture Notes in Physics. Springer-Verlag; 1990. p. 35–50.
[30] Leibovich S. The structure of vortex breakdown. Annu Rev Fluid Mech 1978;10:221–46.
[31] Leibovich S, Kribus A. Large-amplitude wavetrains and solitary waves in vortices. J Fluid Mech 1990;216:459–509.
[32] Lucca-Negro O, O'Doherty T. Vortex breakdown: a review. Prog Energy Comb Sci 2001;27:431–81.
[33] Maxworthy T, Hopfinger E, Redekopp L. Wave motion on vortex cores. J Fluid Mech 1985;151:141–65.
[34] Orlanski I. A simple boundary condition for unbounded hyperbolic flows. J Comput Phys 1976;21:251–69.
[35] Pauley L, Moin P, Reynolds W. The structure of two-dimensional separation. J Fluid Mech 1990;220:397–411.
[36] Perot J. An analysis of the fractional step method. J Comput Phys 1993;108:51–8.
[37] Perot J. Comments on the fractional step method (Letter to the Editor) J Comput Phys 1995;121:190–1.
[38] Rai M, Moin P. Direct simulations of turbulent flow using finite-difference schemes. J Comput Phys 1991;96:15–53.
[39] Rowley C, Colonius T. Discretely nonreflecting boundary conditions for linear hyperbolic systems. J Comput Phys 2000;157:500–38.
[40] Ruith M. Direct numerical simulation and stability analyses of three-dimensional swirling jets and wakes exhibiting vortex breakdown. PhD thesis, Department of Aerospace and Mechanical Engineering, USC, 2002.

[41] Salvetti M, Orlandi P, Verzicco R. Numerical simulations of transitional axisymmetric coaxial jets. AIAA J 1996;34(4):736–43.
[42] Snyder D, Spall R. Numerical simulation of bubble-type vortex breakdown within a tube-and-vane apparatus. Phys Fluids 2000;12(3):603–8.
[43] Spall R, Gatski T. A computational study of the topology of vortex breakdown. Proc R Soc Lond A 1991;435:321–37.
[44] Spall R, Gatski T, Ash R. The structure and dynamics of bubble-type vortex breakdown. Proc R Soc Lond A 1990;429:613–37.
[45] Spall R, Gatski T, Grosch C. A criterion for vortex breakdown. Phys Fluids 1987;30(11):3434–40.
[46] Spall R, Snyder D. Numerical simulations of vortex breakdown: review and recent developments. Recent Res Devel Heat, Mass Moment Transfer 1999;2:41–70.
[47] Verzicco R, Orlandi P. A finite-difference scheme for three-dimensional incompressible flows in cylindrical coordinates. J Comput Phys 1996;123:402–14.